



Cite this: *RSC Adv.*, 2024, 14, 37725

# Fabrication of an $\alpha$ -Fe<sub>2</sub>O<sub>3</sub> NP-modified ZnO NRs/ Ni-foam nanocomposite electrode for electrochemical detection of arsenic in drinking water

Sreymean Ngok,<sup>\*a</sup> Rem Yann,<sup>ad</sup> Chan Oeurn Chey,<sup>c</sup> Xianjie Liu,<sup>b</sup> Magnus Willander<sup>a</sup> and Omer Nur <sup>a</sup>

Arsenic is a toxic contaminant that can be found in drinking water. In this study, the development of an efficient electrode as an electrochemical sensor to detect arsenic(v) in drinking water is presented. The surface of ZnO nanorods (NRs) synthesized on a Ni-foam substrate was modified by depositing  $\alpha$ -Fe<sub>2</sub>O<sub>3</sub> nanoparticles (NPs) to fabricate an electrode for the detection of arsenic(v) contamination in drinking water. This electrode was synthesized through two separate growth steps: a hydrothermal (ZnO NRs) step followed by the dip-coating method ( $\alpha$ -Fe<sub>2</sub>O<sub>3</sub> NPs). The dip-coating method was repeated multiple times, 2 times (ZNF-2), 3 times (ZNF-3) and 4 times (ZNF-4), in order to achieve a uniform coverage of the ZnO NR surface. The electrodes were characterized using XRD, XPS, SEM and UV-vis spectroscopy. The best efficiency among the  $\alpha$ -Fe<sub>2</sub>O<sub>3</sub>NP-modified nanorod samples was observed for the 3-time dip-coated ZNF-3 sample, which presented a uniform and homogeneous morphology, as observed from the SEM images, accompanied with the highest oxidation current. The electrochemical performance of the sensor electrodes was tested for a wide range of arsenic(v) concentrations from 0 to 50 ppb and was monitored using cyclic voltammetry. The results demonstrated a calibration plot that was linear over a concentration range of 0–50 ppb of arsenic(v), and the regression equation extracted from the calibration curve was found to be  $y = 0.003x - 0.6271$  (with  $R^2 = 0.991$ ). The limit of detection (LOD) and limit of quantification (LOQ) were found to be 4.12 ppb and 13.74 ppb, respectively, which are lower than the maximum allowed value recommended by the World Health Organization (WHO) for arsenic in drinking water. This reasonable performance of the ZnO NRs/Ni-foam/ $\alpha$ -Fe<sub>2</sub>O<sub>3</sub>NP nanocomposite electrode can be further enhanced, and the electrode can be utilized for efficient arsenic(v) detection in drinking water.

Received 20th October 2024  
Accepted 12th November 2024

DOI: 10.1039/d4ra07509a

rsc.li/rsc-advances

## 1 Introduction

Arsenic is known as a naturally occurring toxic element and is considered one of the world's environment hazardous agents.<sup>1</sup> Arsenic is generally found in two forms, arsenite (As(III)) and arsenate (As(V)), which are among the inorganic forms of arsenic and the predominant toxic species found in natural drinking water.<sup>2</sup> The World Health Organization has fixed the maximum contaminant level of arsenic in drinking water at 50–

10 ppb.<sup>3–5</sup> Therefore, the detection of the trace amount of arsenic has received considerable attention.

Metal oxide nanomaterials have more sensing ability than single-crystalline bulk semiconductor metal oxide.<sup>6</sup> Furthermore, they exhibit many attractive features such as high chemical and thermal stability, high surface area to volume ratio, tunable electronic states, quantum confinement, high electron mobility, and excellent catalytic properties.<sup>7</sup> Various types of metal oxide nanomaterials have been explored for sensing applications, *e.g.* tin oxide (SnO<sub>2</sub>), indium oxide (In<sub>2</sub>O<sub>3</sub>), zinc oxide (ZnO), tungsten trioxide (WO<sub>3</sub>), cuprous oxide (Cu<sub>2</sub>O), cobalt oxide (Co<sub>3</sub>O<sub>4</sub>) and hematite ( $\alpha$ -Fe<sub>2</sub>O<sub>3</sub>).<sup>8,9</sup> ZnO and  $\alpha$ -Fe<sub>2</sub>O<sub>3</sub> are interesting oxides that are abundant, can be achieved using low cost synthesis methods and are considered less toxic materials.<sup>10,11</sup> Further, different nanocomposites of these oxides with promising synergistic advantageous properties have been reported. Among these nanocomposite materials, ZnO nanostructures modified with  $\alpha$ -Fe<sub>2</sub>O<sub>3</sub> nanostructures have been effective.<sup>12–16</sup> The composition of

<sup>a</sup>Department of Science and Technology, Physics Electronics and Mathematics, Linköping University, SE-60174 Norrköping, Sweden. E-mail: sreymean.ngok@liu.se; Tel: +46 11 36 32 19

<sup>b</sup>Laboratory of Organic Electronics, ITN, Linköping University, Norrköping, SE-60174, Sweden

<sup>c</sup>Graduate School of Science, Royal University of Phnom Penh, Phnom Penh, Cambodia

<sup>d</sup>Department of Physics, Faculty of Science, Royal University of Phnom Penh, Phnom Penh, Cambodia



$\alpha$ -Fe<sub>2</sub>O<sub>3</sub> and ZnO nanostructures results in their synergistic effect, which can enhance the performance of the composite nanomaterial.<sup>7,17–20</sup> These nanocomposites have gained interest in the field of sensor development due to their small dimensions, simplicity of the synthesis procedure, and the possibility of fast sensor response.<sup>21–24</sup> However, these nanomaterials can have some disadvantages, such as low sensitivity, poor selectivity and high operating temperatures, which discourage their utilization in different fields.<sup>24,25</sup> Thus, many researchers have made efforts to improve the sensitivity and selectivity of these metal oxides by compositing them with other metal oxide semiconductors.<sup>9,26–31</sup> In this regard, we have fabricated  $\alpha$ -Fe<sub>2</sub>O<sub>3</sub> nanoparticles on the surface of ZnO NRs grown on a nickel foam substrate in this work for the detection of arsenic(v) in drinking water. The nickel foam substrate has loose porosity, good stability and uniform heat transfer.<sup>32</sup> In addition, nickel foam is a commercial material with a 3D porous structure and can be utilized as an efficient electrode/substrate material as it provides excellent electrical conductivity and a large enough surface area, enabling good access for ions and electrons to reach the active surface of the hybrid composite electrode.<sup>33,34</sup> Moreover, Nickel foam substrates can be used not only to enhance the conductivity performance and promote the penetration of electrolytes in practical applications, but nickel foam has also been used as a current collector in various electrochemical systems, including energy storage devices, chemical sensors and wastewater treatment systems.<sup>35–37</sup>

Herein, we fabricated  $\alpha$ -Fe<sub>2</sub>O<sub>3</sub>NPs on ZnO NRs/Ni-foam substrate for efficient arsenic(v) detection in drinking water. The ZnO NRs/Ni-foam/ $\alpha$ -Fe<sub>2</sub>O<sub>3</sub>NPs nanocomposite electrode was grown *via* two separate growth steps: hydrothermal reaction followed by a dip-coating process. The dip-coating step was optimized by carrying the dipping cycles. The structural and optical properties of the fabricated electrode were then characterized using different techniques, such as XRD, XPS, SEM and UV-vis spectroscopy. The electrochemical performance of the sensor electrode in arsenic(v) detection was investigated by cyclic voltammetry in various electrolytes to achieve efficient detection of arsenic(v). The performance of the ZnO NRs/Ni-foam/ $\alpha$ -Fe<sub>2</sub>O<sub>3</sub>NP nanocomposite electrode in the detection of arsenic(v) in drinking water is promising, verifying it as an excellent candidate that can further be developed to enhance detection efficiency.

## 2 Experimental methods

### 2.1 Materials

Zinc nitrate hexahydrate (Zn(NO<sub>3</sub>)<sub>2</sub>·6H<sub>2</sub>O), hexamethylenetetramine (HMT), iron(III) nitrate nonahydrate (Fe(NO<sub>3</sub>)<sub>3</sub>·9H<sub>2</sub>O) and arsenic standard solutions were purchased from Sigma Aldrich. Nickel foams (10 mm × 15 mm × 1.5 mm) were purchased from Redox.me (Sweden). All chemicals were of analytical grade and used without further purification.

### 2.2 Fabrication of ZnO NRs/Ni-foam and the ZnO NRs/Ni-foam/ $\alpha$ -Fe<sub>2</sub>O<sub>3</sub>NPs nanocomposite

The electrode was fabricated in two steps. During the first step, ZnO NRs were grown *via* the hydrothermal method. Briefly, the

nickel foam substrate was cut into small pieces (10 mm × 15 mm × 1.5 mm), cleaned sequentially with deionized water, acetone, and isopropanol in an ultrasonic bath for 10 minutes each and then dried under a nitrogen flow at room temperature. The cleaned substrates were dip-coated using a seed layer of ZnO nanoparticles for 5 minutes. The seed layer-coated substrates were annealed at 120 °C for 20 min. The seed solution was prepared by dissolving zinc acetate dihydrate (0.01 M) in methanol (125 mL) under vigorous stirring at a temperature of about 60 °C. Subsequently, a 0.03 M solution of KOH (65 mL) in methanol was added dropwise at 60 °C. The mixture was stirred for 2 h at 60 °C and then at room temperature for 12 h to obtain the desired rod-shaped particles.<sup>38</sup> The precursor solution used to synthesize the ZnO NRs was an equal molar (0.05 M) solution of Zn(NO<sub>3</sub>)<sub>2</sub>·6H<sub>2</sub>O and HMT in 100 mL deionized water. Finally, the annealed nickel foam substrates were fixed to a sample holder with the ZnO-seeded sides pointing downwards and dipped into the ZnO precursor solution. After that, the beaker containing the precursor solution and the seeded samples was closed using aluminum foil and baked in an electronic oven at a temperature of 95 °C for 5 h. After the completion of the growth period, the samples were taken out from the oven, washed with deionized water, and then dried using a nitrogen flow. In the second step,  $\alpha$ -Fe<sub>2</sub>O<sub>3</sub> NPs were synthesized by the dip-coating method. The modification of ZnONRs/Ni-foam substrate with  $\alpha$ -Fe<sub>2</sub>O<sub>3</sub> NPs was achieved by dipping the as-grown ZnONRs/Ni-foam into a precursor solution of 0.06 g Fe(NO<sub>3</sub>)<sub>3</sub>·9H<sub>2</sub>O dissolved in 20 mL of deionized water. The products were dipped for 2 minutes per cycle; the dipping process was repeated two, three or four times, and the samples were denoted as (ZNF-2), (ZNF-3) and (ZNF-4), respectively. This was followed by drying under flowing nitrogen at room temperature. The final products were annealed at 400 °C for 2 h in an air environment to convert the hydroxyl-containing phase of Fe<sub>2</sub>O<sub>3</sub> to pure  $\alpha$ -phase (Fig. 1).

### 2.3 General characterization techniques

The morphology of the electrodes was characterized by field-emission scanning electron microscopy (FESEM, Sigma 500 Gemini) with the field-emission gun operated at 10 kV. The structure and phase of the grown nanocomposite were

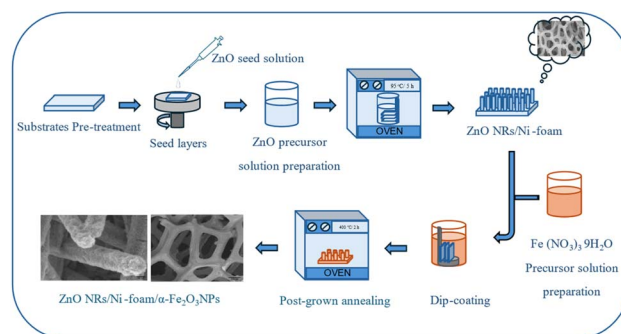


Fig. 1 Schematic showing the process for synthesis of the ZnO NRs/Ni-foam/ $\alpha$ -Fe<sub>2</sub>O<sub>3</sub>NPs nanocomposite electrode.



investigated by powder X-ray diffraction (XRD) using a Philips powder diffractometer equipped with Cu K $\alpha$  radiation at a voltage of 45 kV and a current of 40 mA. The optical properties were analyzed using a UV-vis spectrophotometer (PerkinElmer Lambda 900). The oxidation states and chemical composition were analyzed by X-ray photoelectron spectroscopy (XPS).

## 2.4 Electrochemical characterizations

The electrochemical measurements were carried out using an Autolab potentiostat (Metrohm). The electrochemical properties were measured in a three-electrode configuration composed of Ag/AgCl (3 M KCl) as the reference electrode, platinum wire as the counter electrode and ZnO NRs/ $\alpha$ -Fe $_2$ O $_3$  nanoparticles as the working electrode. The geometric area of the working electrode was estimated to be 0.3 cm $^2$ . The supporting electrolyte was a 1 M KOH solution with arsenic. All measurements were made in a fume hood at room temperature.

## 3 Results and discussion

### 3.1 Morphological analysis

The surface morphology of the ZnO NRs/Ni-foam/ $\alpha$ -Fe $_2$ O $_3$ NPs nanocomposite was examined by FESEM. Fig. 2a and b show the FESEM images of the bare Ni-foam substrate, while (Fig. 2c–f) show the morphology after the growth of the nanorods. Fig. 2f shows a high-magnification FESEM image of the ZnO NRs grown on the nickel foam substrate, demonstrating the expected hexagonal shape. The ZnO NRs were dense highly uniform, and relatively vertically aligned. Fig. 2g–l demonstrate that the  $\alpha$ -Fe $_2$ O $_3$  NPs were deposited on the ZnO NRs. The surfaces of the ZnO NRs modified with  $\alpha$ -Fe $_2$ O $_3$  NPs using different cycles (2, 3 and 4) of dip coating are shown in Fig. 2(g, h), (i, j) and (k, l), respectively. The ZnO NRs surface immersed 2 times in the  $\alpha$ -Fe $_2$ O $_3$  NPs precursor solution for 2 minutes indicated partial covering of the ZnONRs surface with  $\alpha$ -Fe $_2$ O $_3$  nanoparticles (Fig. 2g and h). However, the ZnO NR surface immersed 3 times in the  $\alpha$ -Fe $_2$ O $_3$  NPs precursor solution for 2 minutes each showed full coverage, with gaps between the ZnO NRs (Fig. 2i and j). Furthermore, the gaps between the ZnO NRs were filled with  $\alpha$ -Fe $_2$ O $_3$  NPs after immersing the NRs 4 times in the precursor solution for 2 minutes each (Fig. 2k and l).

### 3.2 Optical properties

The optical characterization of the sample was carried out by UV-visible spectroscopy. In Fig. 3a and b, the absorption *versus* wavelength plots of the  $\alpha$ -Fe $_2$ O $_3$ NP-coated samples obtained by varying the number of dip-coating cycles are displayed. The sample synthesized with 2, 3 and 4 dip-coating cycles of pure ZnO NRs/Ni-foam showed different reflectance values in the visible-light region. ZNF-2, ZNF-3 and ZNF-4 were found to have bandgap energies of approximately 2.05 eV, 1.59 eV and 1.85 eV, respectively, as shown in Fig. 3b. The sample dip-coated 3 times showed the highest absorption in the visible-light region. In Fig. 3c, bare ZnO NRs/Ni-foam shows strong absorption in the ultraviolet range, but there is also fluctuation in light absorption in the 200–400 nm region, with broadening of the optical

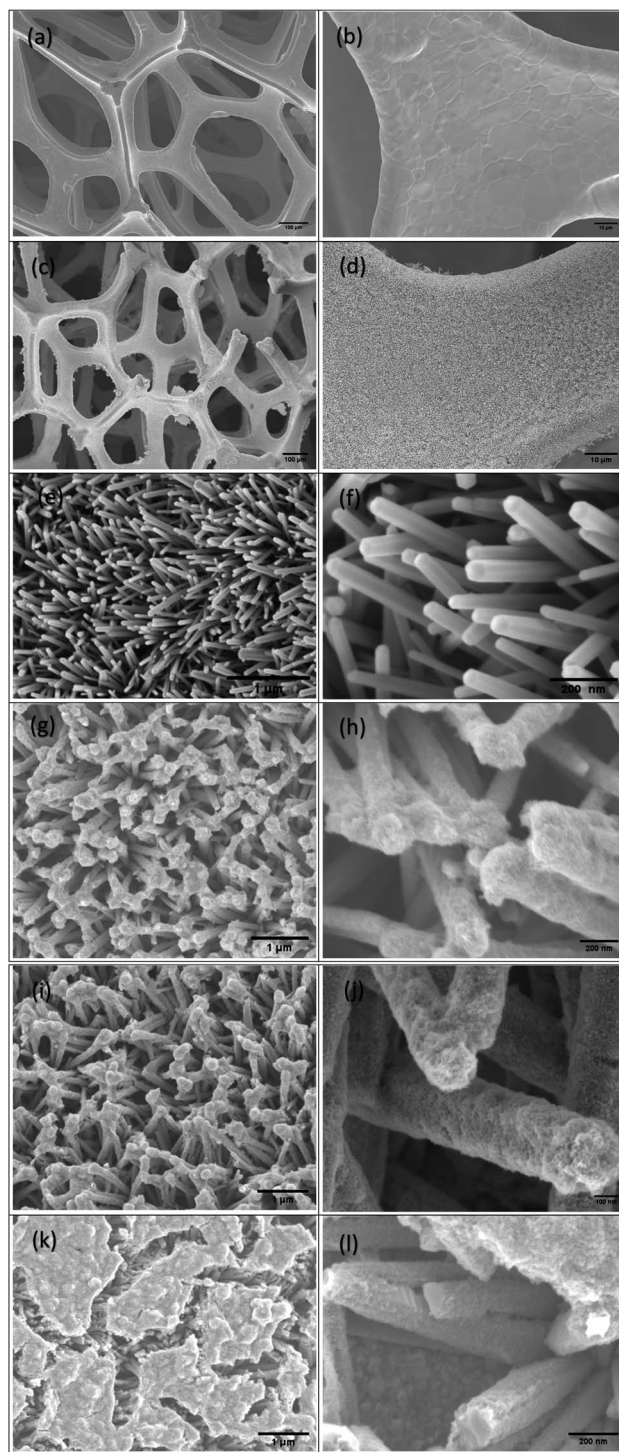


Fig. 2 The SEM images of (a and b) the nickel foam substrate, (c–f) ZnO NRs/Ni-foam and ZnONRs/Ni-foam/ $\alpha$ -Fe $_2$ O $_3$ NPs (ZNF-2) (g and h), (ZNF-3) (i and j) and (ZNF-4) (k and l).

band. However, the spectrum of ZnONRs/Ni-foam/ $\alpha$ -Fe $_2$ O $_3$ NPs shows a characteristic absorption edge at 317 nm and a broader absorption range extending to the visible light region. With an increase in the  $\alpha$ -Fe $_2$ O $_3$  NPs layer thickness, there was an increase in the optical absorption coefficient of the ZnO NRs/Ni-



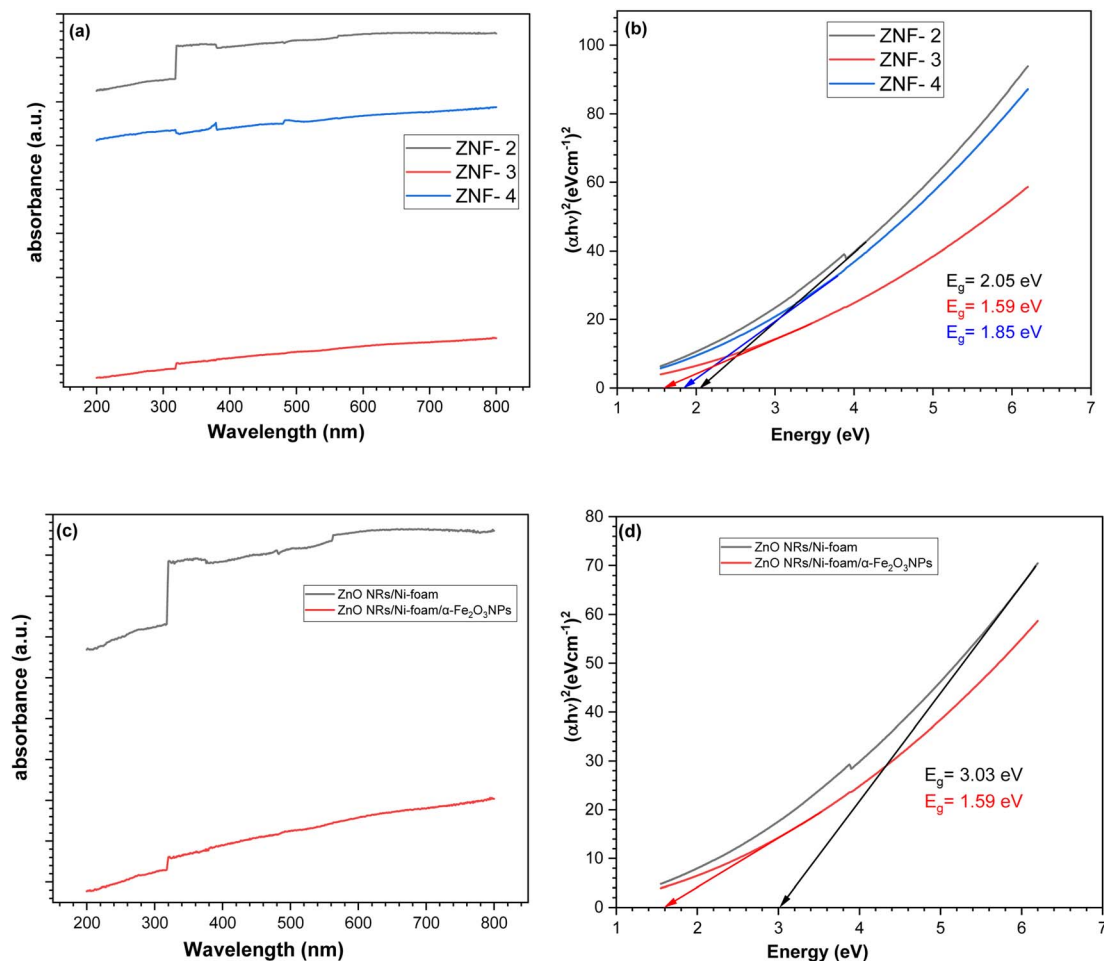


Fig. 3 UV-vis absorption spectra of (a) the ZnO NRs/Ni-foam/ $\alpha$ -Fe<sub>2</sub>O<sub>3</sub>NPs nanocomposite with different dip coatings. (b) Evaluation of bandgap energies of (ZNF-2), (ZNF-3) and (ZNF-4). (c and d) UV-vis absorption spectra and evaluation of bandgap energies of the bare ZnO NRs/Ni-foam and ZnO NRs/Ni-foam/ $\alpha$ -Fe<sub>2</sub>O<sub>3</sub>NPs nanocomposite.

foam/ $\alpha$ -Fe<sub>2</sub>O<sub>3</sub>NPs samples at longer wavelengths compared to ZnO NRs/Ni-foam. ZnO NRs/Ni-foam and the ZnO NRs/Ni-foam/ $\alpha$ -Fe<sub>2</sub>O<sub>3</sub>NPs nanocomposite revealed bandgap energies of approximately 3.03 eV and 1.59 eV, respectively, as shown in Fig. 3d.

### 3.3 XRD analysis

The crystallinity and phase purity of ZnONRs/Ni-foam and ZnONRs/Ni-foam/ $\alpha$ -Fe<sub>2</sub>O<sub>3</sub>NPs were characterized by X-ray diffraction (XRD), as shown in Fig. 4a. The XRD pattern of the bare Ni-foam was recorded from 20° to 90°. The diffraction

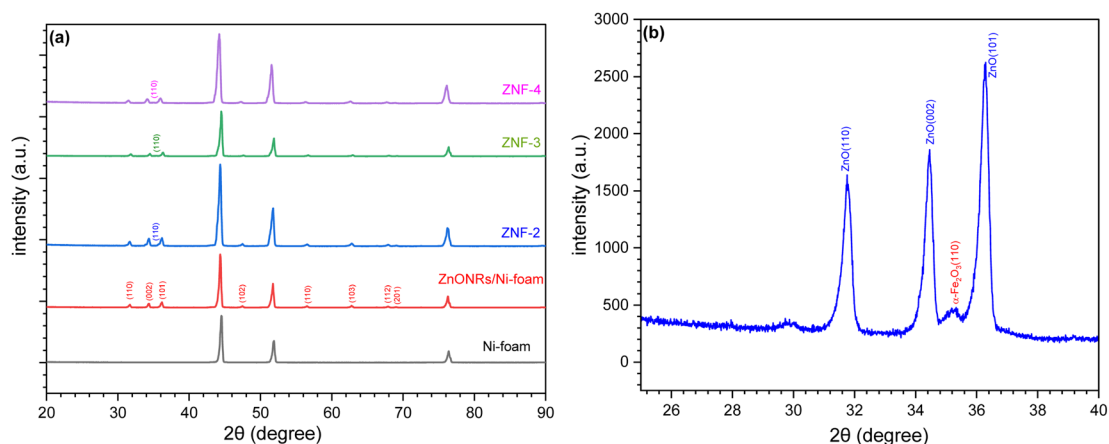


Fig. 4 (a) XRD patterns of Ni-foam, ZnO NRs/Ni-foam, (ZNF-2), (ZNF-3) and (ZNF-4). (b) High-resolution XRD pattern of ZNF-3.



peaks of bare Ni-foam at  $44.50^\circ$ ,  $51.89^\circ$  and  $76.41^\circ$  match well with the standard JCPDS card (JCPDS no.: 003-1051). The diffraction peaks of ZnONRs/Ni-foam at  $2\theta$  positions  $31.66^\circ$ ,

$34.40^\circ$ ,  $36.15^\circ$ ,  $47.50^\circ$ ,  $56.58^\circ$ ,  $62.78^\circ$ ,  $67.93^\circ$  and  $69.02^\circ$  attributed to the (110), (002), (101), (102), (110), (103), (112) and (201) planes, respectively, were due to the hexagonal

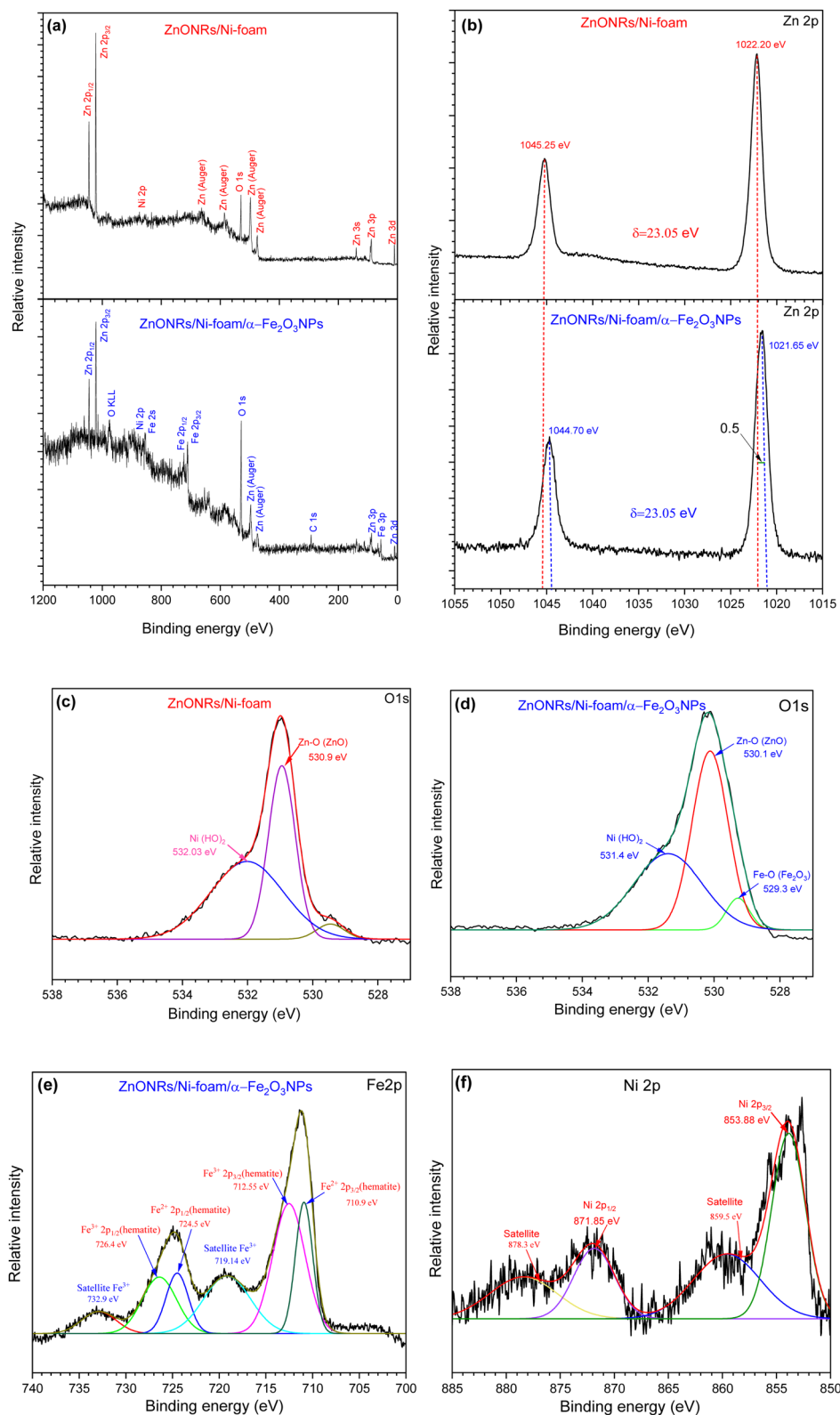


Fig. 5 XPS analysis of the ZnO NRs/Ni-foam and ZnO NRs/Ni-foam/ $\alpha$ -Fe<sub>2</sub>O<sub>3</sub> NPs nanocomposite: (a) survey spectra; high-resolution (b) Zn 2p, (c and d) O 1s, and (e) Fe 2p spectra; (f) Ni 2p spectrum of the nickel foam substrate.

wurtzite structure of the ZnO NRs grown on the nickel foam surface and matched JCPDS no. 00-005-0664 in the diffraction database. The additional diffraction peaks of the ZnO NRs/Ni-foam/ $\alpha$ -Fe<sub>2</sub>O<sub>3</sub>NPs nanocomposite samples obtained 2 (ZNF-2), 3 (ZNF-3) and 4 cycles (ZNF-4) of dip coating were at 35.27°, corresponding to the (110) reflection planes of the rhombohedral structure of the  $\alpha$ -Fe<sub>2</sub>O<sub>3</sub> NPs, and matched the JCPDS: 00-033-0664 file from the diffraction database, as shown in Fig. 4b.

### 3.4 XPS analysis

X-ray photoelectron spectroscopy (XPS) measurements were carried out to investigate the chemical bonding states and elemental composition of ZnO NRs/Ni-foam and the ZnO NRs/Ni-foam/ $\alpha$ -Fe<sub>2</sub>O<sub>3</sub> NPs nanocomposite samples; the results were fitted by a Gaussian fitting method and are shown in Fig. 5. In Fig. 5a, the survey spectrum of bare ZnO NRs/Ni-foam is shown. It confirms the presence of Zn 3d, 3p, 3s, 2p, auger, O 1s and Ni 2p. After the modification of the ZnONRs/Ni-foam surface by depositing  $\alpha$ -Fe<sub>2</sub>O<sub>3</sub> NPs, the survey spectrum included peaks of Fe 3p, 2p, 2s, 0 KLL, and C 1s.<sup>39–42</sup> The high-resolution Zn 2p spectra of the samples are shown in Fig. 5b; doublet peaks are observed at binding energies of 1022.20 eV and 1045.25 eV corresponding to pure ZnONRs/Ni-foam. This is consistent with the oxidation states of Zn 2p<sub>3/2</sub> and Zn 2p<sub>1/2</sub>, respectively. However, these oxidation states were shifted to binding energies of 1021.65 eV and 1044.70 eV, respectively, for the ZnO NRs/Ni-foam/ $\alpha$ -Fe<sub>2</sub>O<sub>3</sub> NPs nanocomposite sample. Moreover, a spin-orbit energy separation of 23.05 eV demonstrates that ZnO had the wurtzite crystal structure (hexagonal),<sup>43,44</sup> which is also consistent with the XRD result. The O 1s core-level XPS spectra of pure ZnO NRs/Ni-foam and the ZnO NRs/Ni-foam/ $\alpha$ -Fe<sub>2</sub>O<sub>3</sub>-NPs nanocomposite samples shown in Fig. 5c and d exhibit peaks at binding energies 530.9 eV and 530.1 eV, corresponding to the bonding of ZnO in the ZnONRs/Ni-foam and ZnO NRs/Ni-foam/ $\alpha$ -Fe<sub>2</sub>O<sub>3</sub>NPs nanocomposite samples, respectively.<sup>45,46</sup> The negative shift of the Zn 2p (by −0.5 eV towards the lower binding energy region) and O 1s peaks indicates that a heterojunction was formed by interfacial interaction in the ZnONRs/Ni-foam/ $\alpha$ -Fe<sub>2</sub>O<sub>3</sub>NP nanocomposite.<sup>47–52</sup> The other fitted peaks of the high-resolution O 1s spectrum of the ZnO NRs/Ni-foam/ $\alpha$ -Fe<sub>2</sub>O<sub>3</sub>NPs nanocomposite located at binding energies 529.3 eV and 531.4 eV could be attributed to Fe–O(Fe<sub>2</sub>O<sub>3</sub>) and Ni(H<sub>2</sub>O), as shown in Fig. 5d.<sup>53</sup> Meanwhile, the peak at 531.4 eV is characteristic of H<sub>2</sub>O, which can be crystal water or water adsorbed on the samples from the air, and it shifted to 532.03 eV in the case of bare ZnO NRs/Ni-foam.<sup>36</sup> The core-level Fe 2p spectra showed Fe<sup>2+</sup> 2p<sub>3/2</sub>, Fe<sup>3+</sup> 2p<sub>3/2</sub>, Fe<sup>2+</sup> 2p<sub>1/2</sub> and Fe<sup>3+</sup> 2p<sub>1/2</sub> peaks at 710.9 eV, 712.55 eV, 724.5 eV and 726.4 eV, respectively, as displayed in Fig. 5e, indicating the presence of Fe<sup>2+</sup> and Fe<sup>3+</sup> species.<sup>40,54</sup> Additionally, two satellite peaks were observed at 719.14 eV and 732.9 eV.<sup>55,56</sup> Fig. 5f shows the Ni 2p<sub>3/2</sub> and Ni 2p<sub>1/2</sub> XPS peaks at 853.88 eV and 871.85 eV, corresponding to the metallic Ni foam substrate.<sup>39,40,57,58</sup> Based on the XRD and XPS results, it was concluded that  $\alpha$ -Fe<sub>2</sub>O<sub>3</sub>NPs-modified ZnO NRs were successfully grown on the nickel foam substrate.

### 3.5 Electrochemical behaviors

**3.5.1 Cyclic voltammetry analysis.** Cyclic voltammetry (CV) measurements of bare ZnO NRs/Ni-foam and the ZnO NRs/Ni-foam/ $\alpha$ -Fe<sub>2</sub>O<sub>3</sub> NPs nanocomposite were performed in 100 mL electrochemical cells to investigate the electrochemical behavior of the electrode material using 70 mL of a 1 M KOH solution and arsenic(v) at different concentrations. The CV curves were recorded in a potential window ranging from −0.4 to 0.6 V vs. Ag/AgCl at a scan rate of 100 mV s<sup>−1</sup> in the 1 M KOH electrolyte. The oxidation and reduction reactions at the working electrode surface are shown by the CV profiles in Fig. 6a. The CV profiles of bare ZnO NRs/Ni-foam and the ZnO NRs/Ni-foam/ $\alpha$ -Fe<sub>2</sub>O<sub>3</sub>NPs nanocomposites obtained after different dip-coating cycles showed that the oxidation and reduction peak currents were higher for the nanocomposite. The highest current was observed in ZnO NRs/Ni-foam/ $\alpha$ -Fe<sub>2</sub>-O<sub>3</sub>NPs nanocomposites, of which ZNF-2 showed a lower current than ZNF-3 and ZNF-4. However, ZNF-3 and ZNF-4 exhibited the same current. In Fig. 6b, the CV curves of the ZNF-3 electrode at different concentrations of arsenic(v) from 0–50 µg per L (ppb) demonstrate that the oxidation and reduction peak current increased with increasing arsenic(v) concentration in the electrolyte. The maximum oxidation and reduction currents 1.3 mA and −0.45 mA were achieved at voltage values of 0.6 V and 0.28 V, respectively, at 50 ppb arsenic(v) concentration. The calibration plot was found to be linear in a wide concentration range of 0–50 ppb of arsenic(v), and the regression equation extracted from the calibration curve was found to be  $y = 0.003x - 0.6271$  ( $R^2 = 0.991$ ), as shown in Fig. 6c. These findings show the successful detection of arsenic(v) in an aqueous solution by the as-developed electrode. For further quantitative analysis, the limit of detection (LOD) and the limit of quantification (LOQ) of the sensor developed in this work were evaluated. Further, the LOD and LOQ results reported by others are shown in Table 1. The LOD is the minimum amount of analyte detected by the system, while LOQ is the lowest amount of analyte that can be quantitatively measured. The World Health Organization (WHO) has set 50 to 10 ppb as the maximum allowed arsenic content in drinking water.<sup>4,5,64</sup> In this work, the LOD and LOQ of the developed ZnO NRs/Ni-foam/ $\alpha$ -Fe<sub>2</sub>O<sub>3</sub>NPs nanocomposite electrode were calculated using the following equations:

$$\text{LOD} = 3\sigma/S \quad (1)$$

$$\text{LOQ} = 10\sigma/S \quad (2)$$

where  $\sigma$  is the standard deviation, and  $S$  is the slope of the calibration curve of current vs. concentration.<sup>65</sup> From eqn (1) and (2), the calculated LOD and LOQ values of the ZnO NRs/Ni-foam/ $\alpha$ -Fe<sub>2</sub>O<sub>3</sub>NPs nanocomposite electrodes were found to be 4.12 ppb and 13.74 ppb, respectively. Although these values are quite high compared to other methods, the electrode can only detect arsenic levels lower than the maximum value recommended by WHO. These CV measurements were repeated several times, and the ZnO NRs/Ni-foam/ $\alpha$ -Fe<sub>2</sub>O<sub>3</sub>NPs nanocomposite sensor electrode was found to be relatively stable.



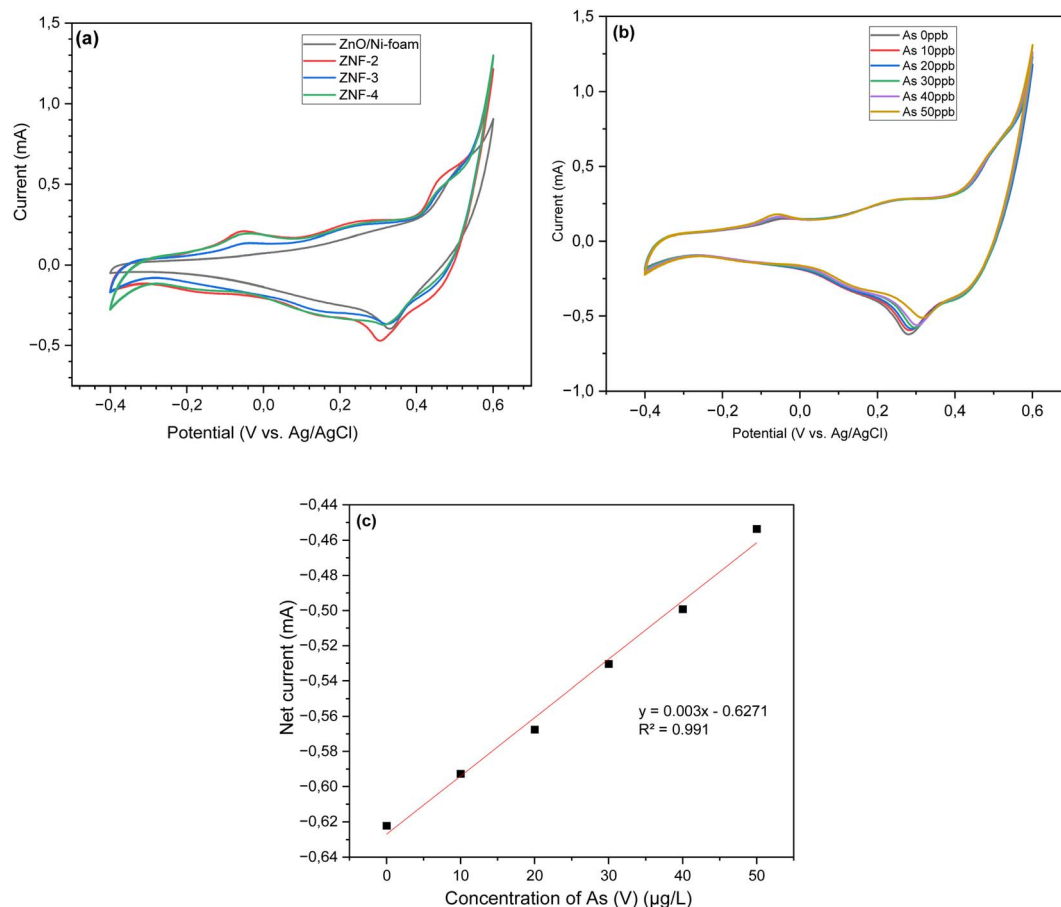


Fig. 6 Cyclic voltammograms of (a) ZnONRs/Ni-foam, (ZNF-2), (ZNF-3) and (ZNF-4) electrodes in a 1 M KOH electrolyte (b). The ZNF-3 electrode at different concentrations of arsenic(v) in the potential range from  $-0.4$  to  $0.6$  V at a scan rate of  $100 \text{ mV s}^{-1}$ ; (c) the corresponding linear calibration plot of net current against arsenic(v) concentration.

Table 1 Comparative study of the performance of different electrochemical sensors developed for arsenic detection

Materials	Detection method	Arsenic concentration	LOD	Ref.
$\text{Fe}_3\text{O}_4$ nanoparticles/nucleobase	SWV	$1.1\text{--}0.5 \text{ }\mu\text{M}$	$0.01 \text{ ppm}$	59
$\text{Fe}_3\text{O}_4$ nanocrystals modified GCE	SWASV	$0.08\text{--}1.54 \text{ }\mu\text{M}$	$0.01 \text{ ppm}$	60
$\text{Fe}_3\text{O}_4$ NPs		$0\text{--}100 \text{ ppb}$	$30 \text{ ppb}$	61
ZnO quantum dots		$10\text{--}100 \text{ ppb}$	$28 \text{ ppb}$	62
ZnO-NRs@Ni-foam	CV	$0.1\text{--}1.0 \text{ }\mu\text{M}$	$0.046 \text{ ppm}$	63
ZnO NRs/Ni-foam/ $\alpha\text{-Fe}_2\text{O}_3$ NPs nanocomposite	CV	$10\text{--}50 \text{ ppb}$	$4.12 \text{ ppb}$	This work

**3.5.2 Interference effect.** The selectivity of a sensor is an important parameter for real aqueous sample applications. The selectivity of the electrode was investigated in the presence of possible interfering metal ions. The effects of different metallic ions, including  $\text{Ag}^+$ ,  $\text{K}^+$ ,  $\text{Cd}^{2+}$ ,  $\text{Zn}^{2+}$  and  $\text{Fe}^{3+}$ , were tested for the possible interference with arsenic detection by the ZnO NRs/Ni-foam/ $\alpha\text{-Fe}_2\text{O}_3$ NPs nanocomposite electrodes under similar experimental conditions. To study the influence of metal ions, metal salts like KCl,  $\text{AgNO}_3$ ,  $\text{Cd}(\text{NO}_3)_2 \cdot 4\text{H}_2\text{O}$ ,  $\text{Zn}(\text{NO}_3)_2 \cdot 6\text{H}_2\text{O}$  and  $\text{Fe}(\text{NO}_3)_3 \cdot 9\text{H}_2\text{O}$  were employed. The concentration of the metal salts was maintained at  $50 \text{ ppb}$  in the  $1 \text{ M KOH}$  electrolyte

solution. There was no strong interaction between arsenic(v) and the interfering species, as shown in Fig. 7. Therefore, these species do not interfere obviously with the electrochemical detection of arsenic(v). The results show that the fabricated sensor has good selectivity towards arsenic(v) ions.

### 3.6 Sensing mechanism of ZnO NRs/Ni-foam/ $\alpha\text{-Fe}_2\text{O}_3$ NPs nanocomposite electrode

The mechanism of electrochemical detection of arsenic(v) by the ZnO NRs/Ni-foam/ $\alpha\text{-Fe}_2\text{O}_3$ NPs nanocomposite electrode is presented in Fig. 8a. The nickel foam substrate facilitates the

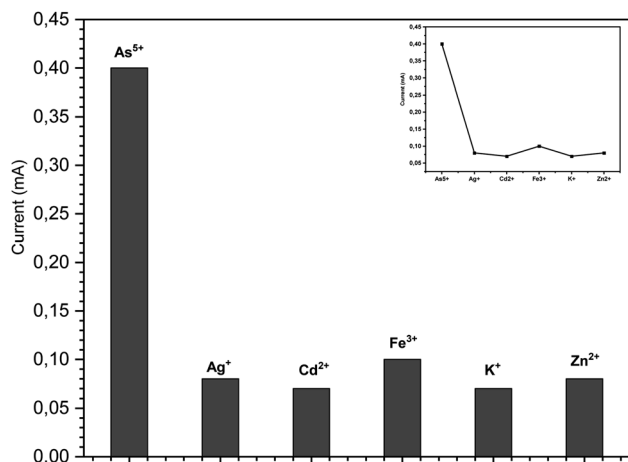
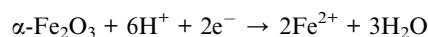


Fig. 7 Interference effect of different metal ions under similar experiment conditions used for the detection of arsenic(v) by the ZnO NRs/Ni-foam/ $\alpha$ -Fe<sub>2</sub>O<sub>3</sub>NP nanocomposite (50 ppb).

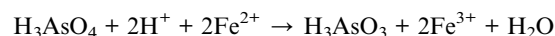
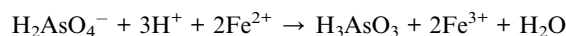
formation of ZnO NRs/ $\alpha$ -Fe<sub>2</sub>O<sub>3</sub>NPs. The structure resembling a flower provides a large surface area and abundant active areas. This facilitates the fast flow of ions and electrons between the electrode and electrolyte. The enhanced performance of the ZnO NRs/Ni-foam/ $\alpha$ -Fe<sub>2</sub>O<sub>3</sub>NPs nanocomposite electrochemical sensor compared with bare ZnO NRs/Ni-foam can be attributed to the distinctive electron transport and high absorption properties of the  $\alpha$ -Fe<sub>2</sub>O<sub>3</sub>NPs in the nanocomposite towards arsenic(v) detection; arsenic(v) ions are adsorbed on the surface of the

working electrode and interact with  $\alpha$ -Fe<sub>2</sub>O<sub>3</sub>NPs during the electrochemical measurement, generating Fe<sup>2+</sup> ions on the electrode surface due to electrochemical reduction.<sup>67</sup> The arsenic(v) detection mechanism on the electrode surface begins with the adsorption of the H<sub>2</sub>AsO<sub>4</sub><sup>−</sup> and H<sub>3</sub>AsO<sub>4</sub> species at the Fe<sup>2+</sup> sites present on the electrode surface. Afterward, the arsenic(v) species are chemically reduced to H<sub>3</sub>AsO<sub>3</sub> by the Fe<sup>2+</sup> ions generated during the electrochemical measurement of the electrode. These reactions can be coupled with another electrochemical step, in which H<sub>3</sub>AsO<sub>3</sub> is reduced to zero-valent arsenic on the electrode surface. Zero-valent arsenic is stripped during the anodic and cathodic scans. The reaction process is demonstrated below.<sup>66</sup>

(1) Reduction of Fe<sup>3+</sup> to Fe<sup>2+</sup> on the electrode surface



(2) Chemical reduction of As(v) to As(III) on the electrode surface:



(3) Electrochemical reduction of As(III) to As (0) on the electrode surface:

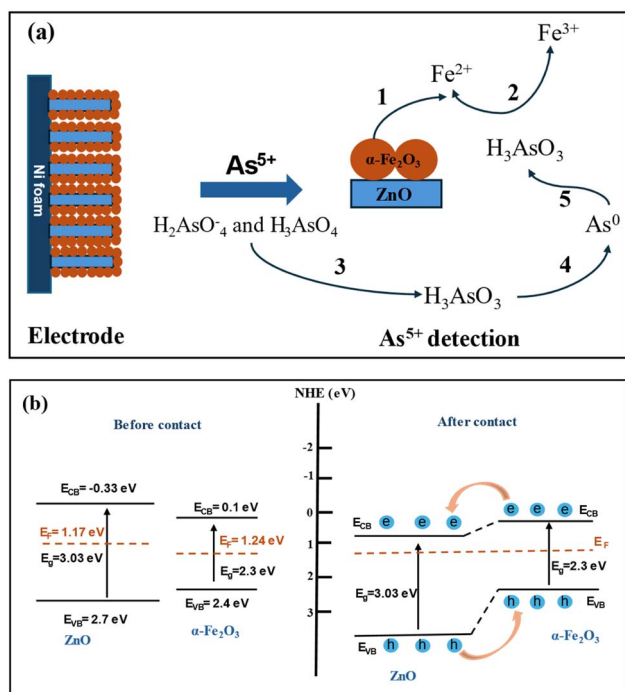
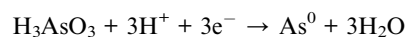


Fig. 8 (a) Schematic of the sensing mechanism (concept based on ref. 66) and (b) equilibrium energy band structure diagram of the ZnO NRs/Ni-foam/ $\alpha$ -Fe<sub>2</sub>O<sub>3</sub>NPs nanocomposite before and after contact between the ZnO NRs and  $\alpha$ -Fe<sub>2</sub>O<sub>3</sub>NPs.

The mechanism of charge separation and transportation in the ZnO NRs/Ni-foam/ $\alpha$ -Fe<sub>2</sub>O<sub>3</sub>NPs nanocomposite can be further explained by the generation of an n-n heterojunction between n-type ZnO and n-type  $\alpha$ -Fe<sub>2</sub>O<sub>3</sub> semiconductors, as shown in Fig. 8b. As the conduction band and valence band of  $\alpha$ -Fe<sub>2</sub>O<sub>3</sub> (0.1 eV and 2.4 eV) are more negative than those of ZnO (−0.33 eV and 2.7 eV), the electrons are transferred from the conduction band of  $\alpha$ -Fe<sub>2</sub>O<sub>3</sub> to ZnO. Meanwhile, the holes in the valence band of ZnO migrate to the valence band of  $\alpha$ -Fe<sub>2</sub>O<sub>3</sub>. This migration and separation of electrons and holes are achieved at the heterojunction interface. When the n-n heterojunction of ZnO NRs/ $\alpha$ -Fe<sub>2</sub>O<sub>3</sub> is in contact with the electrolyte, electrons at the Fermi level align to attain equilibrium. The Fermi level in  $\alpha$ -Fe<sub>2</sub>O<sub>3</sub> is located in between its CB and VB at around 1.24 eV. The Fermi level of n-typical semiconductors generally lies at the bottom of the CB at around 0.1–0.2 eV.<sup>68</sup> As a typical n-type semiconductor, the Fermi level of ZnO is at 1.17 eV. When the semiconductors ZnO and  $\alpha$ -Fe<sub>2</sub>O<sub>3</sub> are joined together, their Fermi levels overlap at 1.24 eV.

## 4 Conclusion

The fabrication of an  $\alpha$ -Fe<sub>2</sub>O<sub>3</sub>NPs-modified ZnONRs/Ni-foam nanocomposite was successfully achieved *via* two separate growth steps using hydrothermal and dip-coating methods. The number of dip-coating cycles was varied to optimize electrode





performance. The ZnO NRs/Ni-foam/ $\alpha$ -Fe<sub>2</sub>O<sub>3</sub>NPs nanocomposite showed the best results when immersed 3 times in the precursor solution, demonstrating the highest oxidation current toward arsenic(v) detection compared with the samples prepared by immersing 2 and 4 times. The electrochemical performance of the optimal electrode in arsenic(v) detection was investigated in a wide range of arsenic concentrations from 0 to 50  $\mu\text{g L}^{-1}$  by cyclic voltammetry. The results demonstrated LOD and LOQ values of 4.12 ppb and 13.74 ppb, respectively; the LOD is lower than the maximum permitted arsenic content recommended by the World Health Organization (WHO) in drinking water. Therefore, the ZnO NRs/Ni-foam/ $\alpha$ -Fe<sub>2</sub>O<sub>3</sub> NPs nanocomposite can be utilized as an electrode to develop efficient arsenic sensor systems for monitoring drinking water.

## Abbreviations

XRD	X-ray diffraction
XPS	X-ray photoelectron spectroscopy
FESEM	Field-emission scanning electron microscopy
ZnO	Zinc oxide
$\alpha$ -Fe <sub>2</sub> O <sub>3</sub>	Hematite
DI	Deionized
UV	Ultraviolet
NRs	Nanorods
NPs	Nanoparticles
CV	Cyclic voltammetry
LOD	Limit of detection
LOQ	Limit of quantification

## Data availability

All data relevant for the reproduction of the results presented in this work are included within the article.

## Author contributions

All authors have contributed to achieve this result, and they are aware and accept the submission.

## Conflicts of interest

The authors declare no conflict of interest.

## Acknowledgements

Authors acknowledge the financial support from the Department of Science and Technology (ITN), Linköping University, as well as ISP and SIDA, Sweden.

## References

- 1 A. Benjamin, R. Hajian, N. Azah and P. Meng, Fabrication of reduced graphene oxide-magnetic nanocomposite (rGO-Fe<sub>3</sub>O<sub>4</sub>) as an electrochemical sensor for trace determination of As (III) in water resources, *J. Electroanal. Chem.*, 2017, **796**, 33–42, DOI: [10.1016/j.jelechem.2017.04.061](https://doi.org/10.1016/j.jelechem.2017.04.061).
- 2 S. Kempahanumakkagari, A. Deep, K. Kim and S. K. Kailasa, Biosensors and Bioelectronics Nanomaterial-based electrochemical sensors for arsenic - A review, *Biosens. Bioelectron.*, 2017, **95**, 106–116, DOI: [10.1016/j.bios.2017.04.013](https://doi.org/10.1016/j.bios.2017.04.013).
- 3 Z. Xie, J. Xu, F. Xie and S. Xiong, Electrochemical detection of as(III) by a rGO/Fe<sub>3</sub>O<sub>4</sub>-modified screen-printed carbon electrode, *Anal. Sci.*, 2016, **32**, 1053–1058, DOI: [10.2116/analsci.32.1053](https://doi.org/10.2116/analsci.32.1053).
- 4 S. Dutta, S. Let, M. M. Shirolkar, A. V. Desai, P. Samanta, S. Fajal, Y. D. More and S. K. Ghosh, A luminescent cationic MOF for bimodal recognition of chromium and arsenic based oxo-anions in water, *Dalton Trans.*, 2021, **50**, 10133–10141, DOI: [10.1039/d1dt01097b](https://doi.org/10.1039/d1dt01097b).
- 5 P. G. Saiz, B. G. Navarrete, S. Dutta, E. Vidal Martín, A. Reizabal, I. Oyarzabal, S. Wuttke, S. Lanceros-Mendez, M. Rosales, A. García and R. Fernandez de Luis, Metal-Organic Frameworks for Dual Photo-Oxidation and Capture of Arsenic from Water, *ChemSusChem*, 2024, 202400592, DOI: [10.1002/cssc.202400592](https://doi.org/10.1002/cssc.202400592).
- 6 F. Hernandez-Ramirez, J. D. Prades, R. Jimenez-Diaz, T. Fischer, A. Romano-Rodriguez, S. Mathur and J. R. Morante, On the role of individual metal oxide nanowires in the scaling down of chemical sensors, *Phys. Chem. Chem. Phys.*, 2009, **11**, 7105–7110, DOI: [10.1039/b905234h](https://doi.org/10.1039/b905234h).
- 7 R. Ahmad, S. M. Majhi, X. Zhang, T. M. Swager and K. N. Salama, Recent progress and perspectives of gas sensors based on vertically oriented ZnO nanomaterials, *Adv. Colloid Interface Sci.*, 2019, **270**, 1–27, DOI: [10.1016/j.cis.2019.05.006](https://doi.org/10.1016/j.cis.2019.05.006).
- 8 C. Wang, L. Yin, L. Zhang, D. Xiang and R. Gao, Metal oxide gas sensors: Sensitivity and influencing factors, *Sensors*, 2010, **10**, 2088–2106, DOI: [10.3390/s100302088](https://doi.org/10.3390/s100302088).
- 9 K. Fan, J. Guo, L. Cha, Q. Chen and J. Ma, Atomic layer deposition of ZnO onto Fe<sub>2</sub>O<sub>3</sub>nanoplates for enhanced H<sub>2</sub>S sensing, *J. Alloys Compd.*, 2017, **698**, 336–340, DOI: [10.1016/j.jallcom.2016.12.203](https://doi.org/10.1016/j.jallcom.2016.12.203).
- 10 B. N. Tiwari, V. V. Mishra and B. Mandal, Synthesis and characterization of ZnO/Fe<sub>2</sub>O<sub>3</sub>composite for electrochemical detection of hydrogen peroxide, *AIP Conf. Proc.*, 2023, **2786**, 3–7, DOI: [10.1063/5.0145432](https://doi.org/10.1063/5.0145432).
- 11 A. Moulahi and F. Sediri, ZnO nanoswords and nanopills: Hydrothermal synthesis, characterization and optical properties, *Ceram. Int.*, 2014, **40**, 943–950, DOI: [10.1016/j.ceramint.2013.06.090](https://doi.org/10.1016/j.ceramint.2013.06.090).
- 12 A. Noruozi and A. Nezamzadeh-Ejchieh, Preparation, characterization, and investigation of the catalytic property of  $\alpha$ -Fe<sub>2</sub>O<sub>3</sub>-ZnO nanoparticles in the photodegradation and mineralization of methylene blue, *Chem. Phys. Lett.*, 2020, **752**, 137587, DOI: [10.1016/j.cplett.2020.137587](https://doi.org/10.1016/j.cplett.2020.137587).
- 13 R. M. Mohamed and A. A. Ismail, Mesoporous  $\alpha$ -Fe<sub>2</sub>O<sub>3</sub>/ZnO heterojunction with a synergistic effect for rapid and efficient reduction of mercury ions, *Sep. Purif. Technol.*, 2021, **266**, 118360, DOI: [10.1016/j.seppur.2021.118360](https://doi.org/10.1016/j.seppur.2021.118360).



- 14 R. Ahmad, M. S. Ahn and Y. B. Hahn, Fabrication of a non-enzymatic glucose sensor field-effect transistor based on vertically-oriented ZnO nanorods modified with Fe<sub>2</sub>O<sub>3</sub>, *Electrochem. Commun.*, 2017, **77**, 107–111, DOI: [10.1016/j.elecom.2017.03.006](#).
- 15 M. Khan, V. Nagal, S. Masrat, T. Tuba, N. Tripathy, M. K. Parvez, M. S. Al-Dosari, A. Khosla, H. Furukawa, A. K. Hafiz and R. Ahmad, Wide-Linear Range Cholesterol Detection Using Fe<sub>2</sub>O<sub>3</sub> Nanoparticles Decorated ZnO Nanorods Based Electrolyte-Gated Transistor, *J. Electrochem. Soc.*, 2022, **169**, 027512, DOI: [10.1149/1945-7111/ac51f6](#).
- 16 M. S. Ahn, R. Ahmad, K. S. Bhat, J. Y. Yoo, T. Mahmoudi and Y. B. Hahn, Fabrication of a solution-gated transistor based on valinomycin modified iron oxide nanoparticles decorated zinc oxide nanorods for potassium detection, *J. Colloid Interface Sci.*, 2018, **518**, 277–283, DOI: [10.1016/j.jcis.2018.02.041](#).
- 17 M. S. Krishna, S. Singh, M. Batool, H. M. Fahmy, K. Seku, A. E. Shalan, S. Lanceros-Mendez and M. N. Zafar, A review on 2D-ZnO nanostructure based biosensors: from materials to devices, *Materials Advances*, 2022, 320–354, DOI: [10.1039/d2ma00878e](#).
- 18 K. S. Bhat, R. Ahmad, T. Mahmoudi and Y. B. Hahn, High performance chemical sensor with field-effect transistors array for selective detection of multiple ions, *Chem. Eng. J.*, 2021, **417**, 128064, DOI: [10.1016/j.cej.2020.128064](#).
- 19 B. Brasiunas, A. Popov, V. Lisyte, A. Kausaite-Minkstiniene and A. Ramanaviciene, ZnO nanostructures: A promising frontier in immunosensor development, *Biosens. Bioelectron.*, 2024, **246**, 115848, DOI: [10.1016/j.bios.2023.115848](#).
- 20 H. Beitollahi, S. Tajik, F. Garkani Nejad and M. Safaei, Recent advances in ZnO nanostructure-based electrochemical sensors and biosensors, *J. Mater. Chem. B*, 2020, **8**, 5826–5844, DOI: [10.1039/d0tb00569j](#).
- 21 S. F. Akhtarianfar, A. Khayatian, R. Shakernejad, M. Almasi-Kashi and S. W. Hong, Improved sensitivity of UV sensors in hierarchically structured arrays of network-loaded ZnO nanorods via optimization techniques, *RSC Adv.*, 2017, **7**, 32316–32326, DOI: [10.1039/c7ra04773h](#).
- 22 N. Tripathy and D. H. Kim, Metal oxide modified ZnO nanomaterials for biosensor applications, *Nano Convergence*, 2018, **5**, DOI: [10.1186/s40580-018-0159-9](#).
- 23 R. Ahmad, M. S. Ahn and Y. B. Hahn, A Highly Sensitive Nonenzymatic Sensor Based on Fe<sub>2</sub>O<sub>3</sub> Nanoparticle Coated ZnO Nanorods for Electrochemical Detection of Nitrite, *Adv. Mater. Interfaces*, 2017, **4**, 1–9, DOI: [10.1002/admi.201700691](#).
- 24 J. H. Yang, K. P. Yuan, L. Y. Zhu, C. Z. Hang, X. X. Li, J. J. Tao, H. P. Ma, A. Q. Jiang and H. L. Lu, Facile synthesis of  $\alpha$ -Fe<sub>2</sub>O<sub>3</sub>/ZnO core-shell nanowires for enhanced H<sub>2</sub>S sensing, *Sens. Actuators, B*, 2020, **307**, 127617, DOI: [10.1016/j.snb.2019.127617](#).
- 25 Y. Wang, Y. Wang, J. Cao, F. Kong, H. Xia, J. Zhang, B. Zhu, S. Wang and S. Wu, Low-temperature H<sub>2</sub>S sensors based on Ag-doped  $\alpha$ -Fe<sub>2</sub>O<sub>3</sub> nanoparticles, *Sens. Actuators, B*, 2008, **131**, 183–189, DOI: [10.1016/j.snb.2007.11.002](#).
- 26 M. Zaki, U. Hashim, M. K. Md Arshad, M. Nasir and A. R. Ruslinda, Sensitivity and selectivity of metal oxides based sensor towards detection of formaldehyde, *IEEE Int. Conf. Semicond. Electron. Proceedings, ICSE. 2016-Septe*, 2016, pp. 312–315, DOI: [10.1109/SMELEC.2016.7573654](#).
- 27 J. Wawrzyniak, Advancements in Improving Selectivity of Metal Oxide Semiconductor Gas Sensors Opening New Perspectives for Their Application in Food Industry, *Sensors*, 2023, **23**, DOI: [10.3390/s23239548](#).
- 28 I. Constantinoiu and C. Viespe, ZnO metal oxide semiconductor in surface acoustic wave sensors: A review, *Sensors*, 2020, **20**, 1–20, DOI: [10.3390/s20185118](#).
- 29 M. L. M. Napi, S. M. Sultan, R. Ismail, K. W. How and M. K. Ahmad, Electrochemical-based biosensors on different zinc oxide nanostructures: A review, *Materials*, 2019, **12**, 1–34, DOI: [10.3390/ma12182985](#).
- 30 Z. Lou, F. Li, J. Deng, L. Wang and T. Zhang, Branch-like hierarchical heterostructure ( $\alpha$ -Fe<sub>2</sub>O<sub>3</sub>/TiO<sub>2</sub>): A novel sensing material for trimethylamine gas sensor, *ACS Appl. Mater. Interfaces*, 2013, **5**, 12310–12316, DOI: [10.1021/am402532v](#).
- 31 S. Ngok, N. Razmi, E. Mustafa, X. Liu, C. O. Chey, M. Willander and O. Nur, Chemical, synthesis, characterization and electrochemical properties of  $\alpha$ -Fe<sub>2</sub>O<sub>3</sub>/ZnO composite nano-heterojunction for sensing application, *Nano Sel.*, 2024, 1–10, DOI: [10.1002/nano.202300155](#).
- 32 F. Gao, Y. Tang, J. Liu, K. Pan, M. Zhou, G. Qian, M. Liu, F. Yu, J. Dan and B. Dai, Nickel foam supported CuCe mixed metal oxide as monolith catalyst for NO removal, *Chem. Eng. J.*, 2023, **474**, 145713, DOI: [10.1016/j.cej.2023.145713](#).
- 33 G. W. Yang, C. L. Xu and H. L. Li, Electrodeposited nickel hydroxide on nickel foam with ultrahigh capacitance, *Chem. Commun.*, 2008, 6537–6539, DOI: [10.1039/b815647f](#).
- 34 D. R. Rolison, J. W. Long, J. C. Lytle, A. E. Fischer, C. P. Rhodes, T. M. Mc Evoy, M. E. Bourg and A. M. Lubers, Multifunctional 3D nanoarchitectures for energy storage and conversion, *Chem. Soc. Rev.*, 2009, **38**, 226–252, DOI: [10.1039/b801151f](#).
- 35 Y. Y. Li, Y. L. Wu, N. Chen, Y. L. Ma, W. X. Ji and Y. G. Sun, Preparation of metal oxide-loaded nickel foam adsorbents modified by biochar for the removal of cationic dyes from wastewater, *Chin. J. Anal. Chem.*, 2023, **51**, 100278, DOI: [10.1016/j.cjac.2023.100278](#).
- 36 J. Hao, X. Wang, F. Liu, S. Han, J. Lian and Q. Jiang, Facile Synthesis ZnS/ZnO/Ni(OH)<sub>2</sub> Composites Grown on Ni Foam: A Bifunctional Materials for Photocatalysts and Supercapacitors, *Sci. Rep.*, 2017, **7**, 1–12, DOI: [10.1038/s41598-017-03200-2](#).
- 37 M. S. Ratsoma, B. L. O. Poho, K. Makgopa, K. Raju, K. D. Modibane, C. J. Jafta and K. O. Oyedotun, Application of Nickel Foam in Electrochemical Systems: A Review, *J. Electron. Mater.*, 2023, **52**, 2264–2291, DOI: [10.1007/s11664-023-10244-w](#).



- 38 C. Pacholski, A. Kornowski and H. Weller, Self-assembly of ZnO: From nanodots to nanorods, *Angew. Chem., Int. Ed.*, 2002, **41**, 1188–1191, DOI: [10.1002/1521-3773\(20020402\)41:7<1188::AID-ANIE1188>3.0.CO;2-5](#).
- 39 T. Xia, Y. Wang, C. Mai, G. Pan, L. Zhang, W. Zhao and J. Zhang, Facile: In situ growth of ZnO nanosheets standing on Ni foam as binder-free anodes for lithium ion batteries, *RSC Adv.*, 2019, **9**, 19253–19260, DOI: [10.1039/c9ra03373d](#).
- 40 S. Thangarasu, N. Baby, M. Bhosale, J. Lee, C. Jeong and T. H. Oh, Fe<sub>2</sub>O<sub>3</sub>/Ni Nanocomposite Electrocatalyst on Cellulose for Hydrogen Evolution Reaction and Oxygen Evolution Reaction, *Int. J. Mol. Sci.*, 2023, **24**, DOI: [10.3390/ijms242216282](#).
- 41 D. Briggs, X-ray photoelectron spectroscopy (XPS), *Handb. Adhes.*, 2nd edn, 2005, pp. 621–622, DOI: [10.1002/0470014229.ch22](#).
- 42 B. Vincent Crist, Commercially Pure Binary Oxides, *Demo Version (172 pages) PDF Handbooks of Monochromatic XPS Spectra Fundamental XPS Data from Pure Elements, Pure Oxides, and Chemical Compounds*, 2005, vol. 2, pp. 1–9.
- 43 M. Claros, M. Setka, Y. P. Jimenez and S. Vallejos, Aacvd synthesis and characterization of iron and copper oxides modified znO structured films, *Nanomaterials*, 2020, **10**, 1–16, DOI: [10.3390/nano10030471](#).
- 44 T. Wang, B. Jin, Z. Jiao, G. Lu, J. Ye and Y. Bi, Photo-directed growth of Au nanowires on ZnO arrays for enhancing photoelectrochemical performances, *J. Mater. Chem. A*, 2014, **2**, 15553–15559, DOI: [10.1039/c4ta02960g](#).
- 45 N. Al-Qasbi, M. T. Soomro, M. Aslam, A. U. Rehman, S. Ali, E. Y. Danish, I. M. I. Ismail and A. Hameed, The efficacy of the ZnO:α-Fe<sub>2</sub>O<sub>3</sub> composites modified carbon paste electrode for the sensitive electrochemical detection of loperamide: A detailed investigation, *J. Electroanal. Chem.*, 2016, **783**, 112–124, DOI: [10.1016/j.jelechem.2016.11.036](#).
- 46 H. Wang, S. Baek, J. Song, J. Lee and S. Lim, Microstructural and optical characteristics of solution-grown Ga-doped ZnO nanorod arrays, *Nanotechnology*, 2008, **19**, DOI: [10.1088/0957-4484/19/7/075607](#).
- 47 Z. Guo, W. Huo, T. Cao, X. Liu, S. Ren, J. Yang, H. Ding, K. Chen, F. Dong and Y. Zhang, Heterojunction interface of zinc oxide and zinc sulfide promoting reactive molecules activation and carrier separation toward efficient photocatalysis, *J. Colloid Interface Sci.*, 2021, **588**, 826–837, DOI: [10.1016/j.jcis.2020.11.118](#).
- 48 L. Cheng, Y. Li, G. Cao, G. Sun, J. Cao and Y. Wang, Boosting TEA sensing performance of ZnO porous hollow spheres via in situ construction of ZnS-ZnO heterojunction, *Sens. Actuators, B*, 2022, **364**, 131883, DOI: [10.1016/j.snb.2022.131883](#).
- 49 S. W. Kang, P. R. Deshmukh, Y. Sohn and W. G. Shin, Plasmonic gold sensitization of ZnO nanowires for solar water splitting, *Mater. Today Commun.*, 2019, **21**, 100675, DOI: [10.1016/j.mtcomm.2019.100675](#).
- 50 F. Qiao, W. Liu, J. Yang, J. Yuan, K. Sun and P. Fei Liu, Hydrogen production performance and theoretical mechanism analysis of chain-like ZnO/ZnS heterojunction, *Int. J. Hydrogen Energy*, 2023, **48**, 953–963, DOI: [10.1016/j.ijhydene.2022.09.246](#).
- 51 T. Wang, B. Jin, Z. Jiao, G. Lu, J. Ye and Y. Bi, Photo-directed growth of Au nanowires on ZnO arrays for enhancing photoelectrochemical, *J. Mater. Chem. A*, 2014, 15553–15559, DOI: [10.1039/c4ta02960g](#).
- 52 X. Liang, X. Wang, M. Yang, H. Dong, Y. Ji and L. Wang, α-Fe<sub>2</sub>O<sub>3</sub>-supported Co<sub>3</sub>O<sub>4</sub> nanoparticles to construct highly active interfacial oxygen vacancies for ozone decomposition, *Environ. Pollut.*, 2023, **330**, 121704, DOI: [10.1016/j.envpol.2023.121704](#).
- 53 Y. Zhong, Y. Ma, Q. Guo, J. Liu, Y. Wang, M. Yang and H. Xia, Controllable synthesis of TiO<sub>2</sub>@Fe<sub>2</sub>O<sub>3</sub> core-shell nanotube arrays with double-wall coating as superb lithium-ion battery anodes, *Sci. Rep.*, 2017, **7**, 1–9, DOI: [10.1038/srep40927](#).
- 54 S. A. Shah, X. Shen, A. Yuan, Z. Ji, X. Yue, G. Zhu, H. Zhou, K. Xu, J. Zhu and Y. Chen, One step in-situ synthesis of Ni<sub>3</sub>S<sub>2</sub>/Fe<sub>2</sub>O<sub>3</sub>/N-doped carbon composites on Ni foam as an efficient electrocatalyst for overall water splitting, *Appl. Surf. Sci.*, 2020, **527**, 146918, DOI: [10.1016/j.apsusc.2020.146918](#).
- 55 S. S. Yi, B. R. Wulan, J. M. Yan and Q. Jiang, Highly Efficient Photoelectrochemical Water Splitting: Surface Modification of Cobalt-Phosphate-Loaded Co<sub>3</sub>O<sub>4</sub>/Fe<sub>2</sub>O<sub>3</sub> p-n Heterojunction Nanorod Arrays, *Adv. Funct. Mater.*, 2019, **29**, 1–9, DOI: [10.1002/adfm.201801902](#).
- 56 X. F. Lu, X. Y. Chen, W. Zhou, Y. X. Tong and G. R. Li, α-Fe<sub>2</sub>O<sub>3</sub>@PANI core-shell nanowire arrays as negative electrodes for asymmetric supercapacitors, *ACS Appl. Mater. Interfaces*, 2015, **7**, 14843–14850, DOI: [10.1021/acsami.5b03126](#).
- 57 N. Li, S. X. Jin, Q. Y. Liao and C. X. Wang, ZnO anchored on vertically aligned graphene: Binder-free anode materials for lithium-ion batteries, *ACS Appl. Mater. Interfaces*, 2014, **6**, 20590–20596, DOI: [10.1021/am507046k](#).
- 58 S. Lu, H. Wang, J. Zhou, X. Wu and W. Qin, Atomic layer deposition of ZnO on carbon black as nanostructured anode materials for high-performance lithium-ion batteries, *Nanoscale*, 2017, **9**, 1184–1192, DOI: [10.1039/c6nr07868k](#).
- 59 S. Sawan, K. Hamze, A. Youssef, K. Bouhadir, A. Errachid, R. Maalouf and N. Jaffrezic-Renault, The Use of Voltammetry for Sorption Studies of Arsenic (III) Ions by Magnetic Beads Functionalized with Nucleobase Hydrazide Derivatives, *Electroanalysis*, 2021, **33**, 1789–1799, DOI: [10.1002/elan.202100150](#).
- 60 X. Z. Yao, Z. Guo, Q. H. Yuan, Z. G. Liu, J. H. Liu and X. J. Huang, Exploiting differential electrochemical stripping behaviors of Fe<sub>3</sub>O<sub>4</sub> nanocrystals toward heavy metal ions by crystal cutting, *ACS Appl. Mater. Interfaces*, 2014, **6**, 12203–12213, DOI: [10.1021/am501617a](#).
- 61 B. Liu and J. Liu, DNA adsorption by magnetic iron oxide nanoparticles and its application for arsenate detection, *Chem. Commun.*, 2014, **50**, 8568–8570, DOI: [10.1039/c4cc03264k](#).



- 62 S. K. Pal, N. Akhtar and S. K. Ghosh, Determination of arsenic in water using fluorescent ZnO quantum dots, *Anal. Methods*, 2016, **8**, 445–452, DOI: [10.1039/c5ay02472b](https://doi.org/10.1039/c5ay02472b).
- 63 M. Rauf, S. K. Shah, A. Algahtani, V. Tirth, A. H. Alghtani, T. Al-Mughanam, K. Hayat, N. H. Al-Shaalan, S. Alharthi, S. A. Alharthy and M. A. Amin, Application of ZnO-NRs@Ni-foam substrate for electrochemical fingerprint of arsenic detection in water, *RSC Adv.*, 2023, **13**, 14530–14538, DOI: [10.1039/d3ra01574b](https://doi.org/10.1039/d3ra01574b).
- 64 Y. Sayato, WHO Guidelines for Drinking-Water Quality, *Eisei Kagaku*, 1989, **35**, 307–312, DOI: [10.1248/jhs1956.35.307](https://doi.org/10.1248/jhs1956.35.307).
- 65 M. Nazari, S. Kashanian and R. Rafipour, Laccase immobilization on the electrode surface to design a biosensor for the detection of phenolic compound such as catechol, *Spectrochim. Acta, Part A*, 2015, **145**, 130–138, DOI: [10.1016/j.saa.2015.01.126](https://doi.org/10.1016/j.saa.2015.01.126).
- 66 E. Toral-Sanchez, J. R. Rangel-Mendez and L. F. Chazaro-Ruiz, Characterization of iron-modified carbon paste electrodes and their application in As(V) detection, *J. Appl. Electrochem.*, 2016, **46**, 205–215, DOI: [10.1007/s10800-015-0903-3](https://doi.org/10.1007/s10800-015-0903-3).
- 67 D. Suter, S. Banwart and W. Stumm, Dissolution of Hydrous Iron(III) Oxides by Reductive Mechanisms, *Langmuir*, 1991, **7**, 809–813, DOI: [10.1021/la00052a033](https://doi.org/10.1021/la00052a033).
- 68 Y. I. Li, Y. Liu, Y. j. Hao, X. j. Wang, R. h. Liu and F. t. Li, Fabrication of core-shell BiVO<sub>4</sub>@Fe<sub>2</sub>O<sub>3</sub> heterojunctions for realizing photocatalytic hydrogen evolution via conduction band elevation, *Mater. Des.*, 2020, **187**, 108379, DOI: [10.1016/j.matdes.2019.108379](https://doi.org/10.1016/j.matdes.2019.108379).

